Sex-Specific DNA-Replication In The Early Mammalian Embryo

Authors

Jason Alexander Halliwell[1]*, Javier Martin-Gonzalez[2], Adnan Hashim[3], John Arne Dahl[3], Eva Ran Hoffmann[1]*, Mads Lerdrup[1]*

Affiliations

[1] DNRF Centre for Chromosome Stability, Department of Cellular and Molecular Medicine, University of Copenhagen, DK-2200 Copenhagen, Denmark

[2] Core Facility for Transgenic Mice, Department of Experimental Medicine, Faculty of Health and Medical Sciences, University of Copenhagen, Denmark

[3] Department of Microbiology, Oslo University Hospital, Rikshospitalet, NO-0372 Oslo, Norway

* Corresponding authors

Abstract

The timing of mammalian DNA replication is crucial for minimizing errors and is influenced locally by genome usage and chromatin states. However, our understanding of replication timing in the unique environment that exists in newly formed mammalian embryos is limited. Here, we performed genome-wide investigations of replication timing in mouse zygotes and 2-cell embryos. We discovered that zygotes lack a conventional replication timing, but a program emerged in 2-cell embryos. Notably, this program differs from embryonic stem cells and shows asynchrony between the parental genomes. We observed late replication of maternal pericentromeric regions and DNA associated with the nuclear lamina in each parental genome, whereas unexpected early replication occurred in regions with histone marks deposited by Polycomb Repressive Complexes on the maternal chromatin. This atypical and asynchronous replication of the two parental genomes may advance our understanding of replication stress in early human embryos and trigger strategies to reduce errors and aneuploidies.

Main

DNA replication is a fundamental process ensuring accurate transfer of genetic information when cells divide. Its precise orchestration follows a well-defined temporal order, known as the replication timing program[1,2]. Replication timing has emerged as a key cellular fingerprint that is associated with various genomic features, such as gene density, gene transcription, histone modifications, DNA methylation, and 3D genome organization[3-8]. Furthermore, it exhibits a remarkable level of synchrony across single cells and their homologous chromosomes[9,10].

Significant advancements in our comprehension of replication timing have been facilitated by a range of sequencing technologies collectively referred to as Repli-seq[9-11]. Repli-seq examines copy number variations of S phase cells and normalizes them against G1 reference cells. More recently, the advent of single-cell sequencing approaches has revolutionized the investigation of Replication timing in individual cells[9,10].

Despite significant progress, our comprehension of replication timing heavily relies on established replication programs derived from *in vitro* cell lines. However, little is known about how *de novo* replication programs are established after fertilization in the developing embryo.

Human and mouse oocytes and embryos are characterized by several transformative changes in their epigenetic landscapes[12-16], and a permissive transcriptional environment that allows for unusually high retrotransposon activity and the emergence of alternative retrotransposon-initiated transcripts[17-20]. As the paternal genome is unpacked from the fertilizing sperm, its protamines are replaced by

histones, and both the maternal and paternal genomes must exit the transcriptionally silenced states that existed in the gametes to initiate embryonic genome activation[21], while undergoing major morphological changes[22]. Collectively, these factors could place the preimplantation genome under considerable exertion, and might contribute to the reported instances of replication stress during the first cellular divisions in mouse and human embryos[23,24]. Consequently, exceptional factors might influence and govern the replication and its timing at the early stages of mammalian embryo development.

Results

Single-embryo Repli-seq reveals atypical replication timing in zygotes and 2-cell embryos

To better understand the mechanisms underlying the establishment of replication timing during early mammalian embryogenesis, we developed a single embryo Repli-seq technique to study replication timing in the zygote and 2-cell stages of mouse embryos (**Fig. 1a**). The reliability of Repli-Seq relies on the precise selection of cells in S phase, therefore, we first employed EdU labeling at specific time points following fertilization. This allowed us to determine the exact timing of the zygotes entry into and exit from the first S phase (**Fig. 1a-c**). For the 2-cell embryos, we additionally used Nocodazole to arrest *in vitro* fertilized mouse zygotes in metaphase for 4 hours, aligning their cell cycles and facilitating precise selection of G1 or S phase cells based on EdU incorporation (**Fig. 1a-c**).

With accurate definition of the cell cycle times, we obtained a cohort of 26 zygotes and 44 *in vitro* fertilized 2-cell stage embryos from C57BL/6N oocytes fertilized with CAST/EiJ sperm. These embryos were processed using a modified version of previously published sc-Repliseq pipelines (methods)[9,10]. To validate the reliability of our approach, we also generated replication timing profiles from individual mouse embryonic stem cells (ESCs). These replication timing profiles demonstrated a strong agreement with the previously published sc-Repli-seq profiles obtained from ESCs (**Extended Data Fig. 1a-e, Supplementary Table 1**)[9]. Based on our previous EdU determination, six, four, seven, and nine zygotes were assigned as G1, early S, mid S, and late S phase, respectively. For 2-cell embryos, seven, eleven, thirteen, and thirteen embryos were assigned to the G1, early S, mid S, and late S phase, respectively.

Our analysis of replication timing in individual 2-cell embryos revealed consistent replication timing profiles across individual samples (**Fig. 1d**). However, we observed marked changes in the overall level of differences between S phase cells and G1 cells during embryonic growth. Specifically, the zygote data exhibited a notably smaller overall deviation (**Fig. 1e,f**), while Repli-Seq profiles, generated from

78 ESCs showed a strong and localized deviation between their S and G1 cells, which was not attributed
79 to read depth (**Fig. 1e-g and Extended Data Fig. 1f-g, Supplementary Table 2**). 2-cell embryos
80 displayed intermediate levels of G1/S deviation, suggesting that the changes might coincide with the
81 embryo genome activation. While asynchronous replication between the two parental genomes is a
82 potential cause, this could also indicate a uniform replication program that initiates from a high
83 abundance of replication origins that are randomly distributed throughout the genome.

84 Notably, when we assessed the replication status of each embryo by methodology previously
85 validated in ESCs[9] (**Fig. 1h,i**), we found a close alignment between the assessment made by EdU
86 incorporation (**Fig. 1b,c**) and the calculated Replication Score for each 2-cell embryos, but not for
87 zygotes (**Fig. 1j, Supplementary Table 3**). Given the limited and insignificant differences between G1
88 and S phase zygotes, (**Fig. 1f,g and Extended Data Fig. 1f**), we decided to focus on the significant
89 deviations seen in the 2-cell stage in our subsequent analyses of genome-wide localization of
90 replication timing.

91 **Consistent differences in local replication timing between 2-cell embryos and ESCs**

92 Although replication timing between our 2-cell embryos and ESCs ordered by the fraction of the
93 genome scored as replicated [9] showed many similarities throughout the genome, we also observed
94 notable local differences between the two cell types (**Fig. 2a**). These distinct differences were
95 consistent across individual samples of the two cell types, with some displaying markedly earlier or
96 later replication in the 2-cell embryos compared to ESCs (**Fig. 2a**).

97 To assess these differences in an unbiased manner and on a global scale, we performed k-means
98 clustering of the genome-wide Repli-seq enrichment of S-phase 2-cell stage embryos and ESCs. This
99 revealed globally organized replication timing patterns recurring within individual cells, with
100 systematic and persistent differences between 2-cell embryos and ESCs (**Fig. 2b-c Supplementary**
101 **Table 4**). In ESCs, both clusters 2 and 3 replicated late, but in 2-cell embryos their replication timing
102 differed (**Fig. 2c-d**). Cluster 3 replicated comparably early in 2-cell embryos and exhibited high
103 transcriptional induction at the 2-cell stage, while the comparably early replicating ESC cluster 9 was
104 associated with high transcription induction at 4 and 8-cell stage[19] (**Fig. 2e-f and Extended Data Fig.**
105 **2a**). Indeed, previous studies have consistently demonstrated that replication timing is associated with
106 local transcriptional potential and chromatin organization[4,25-27].

107 In light of these observations, we sought to investigate the potential influence of maternally inherited
108 epigenetic landscape on the observed differences in replication timing, in addition to transcriptional
109 induction. To accomplish this, we examined the enrichment of epigenetic features using published

110 ChIP-seq, Cut&Run, and ATAC-seq data from Meiosis II (MII) and fully grown oocytes (FGO)[12,13,16,19,28-
111 31] (**Fig. 2g and Extended Data Fig. 2b-c, Supplementary Table 5**). Interestingly, we identified a
112 pronounced global association between replication timing differences and the H2AUb and H3K27me3
113 histone marks deposited by Polycomb Repressive Complexes (PRCs)[13,16,28], which were associated with
114 relatively early replicating regions in the 2-cell embryos compared to ESCs (**Fig. 2g-i and Extended**
115 **Data Fig. 2b,c, 3a,b**). Together, these analyses revealed that inherited maternal histone marks
116 deposited by PRCs are associated with the temporal organization of DNA replication in 2-cell stage
117 embryos.

118 **Abundant local parental differences in the replication timing of 2-cell embryos**

119 To explore whether asynchronous DNA replication timing of the parental haplotypes could explain the
120 smaller G1/S deviation in log2 fold signal between 2-cell embryos and ESC (**Fig. 1h-j, Extended Data**
121 **Fig. 1f,g**), we separated the genomes originating from each of the gametes based on nucleotide
122 variations between the two parental strains. This allowed us to independently visualize and compare
123 the replication timing profiles of the maternal and paternal genome (**Fig. 3a**). Measures of the relative
124 Euclidian distances between Repli-seq values of individual 2-cell and ESC haplotypes as well as
125 hierarchical clustering of these revealed a strikingly distinct DNA replication program in each of the 2-
126 cell haplotypes that was unlike that of ESCs (**Fig. 3b, Extended Data fig. 3c**). Next, we performed k-
127 means clustering of the genome-wide Repli-seq enrichment within the maternal and paternal 2-cell
128 and ESC haplotypes. Based on this, we observed that a large fraction of the genome exhibited
129 consistent earlier replication in the maternal haplotype compared to the paternal haplotype, while
130 the opposite was the case for another large fraction (**Fig. 3c, d, Supplementary Table 6**). These findings
131 in the 2-cell embryo are in contrast to our observations in ESC, where we observed a strong correlation
132 between the replication timing profiles of the two haplotypes, consistent with previous reports (**Fig.**
133 **3e**)[9,10]. Notably, separation of paternal haplotypes did not lead to an increase in the low G1/S deviation
134 in log2 fold signal we observed in the zygotes and only partially increased the G1/S deviation of 2-cell
135 embryos, which was still considerably smaller than that of ESCs (**Fig. 1e-f and Extended Data Fig. 3d,**
136 **e**). This data supports that the lower G1/S deviation observed in zygotes and 2-cell embryos compared
137 to ESCs is not primarily caused by asynchrony between the maternal and paternal genomes. The more
138 uniform progression of replication during early embryogenesis, deviating from the classical temporal
139 pattern, could be the result of actual uniformity or that structures are below our effective resolution.

140 We next investigated whether genomic regions that harbor high transcriptional induction at the 2-cell
141 stage are replicated early across both parental haplotypes. Indeed, regions of high transcriptional
142 induction are replicated early in both parental haplotypes from 4-cell stage onwards, indicating

143 influence from the major embryonic genome activation[19] (**Fig. 3f, g and Extended Data fig. 3f**). Given
144 the importance of maternal oocyte derived factors in the development of the embryo, we examined
145 the enrichment of histone marks in relation to replication status differences between the parental
146 haplotypes. Notably, the marks H2AUb and in particularly H3K27me3 deposited by PRCs were
147 enriched in early-replicating maternal regions (**Fig. 3h and i, Extended Data Fig. 4a-d**). Indeed, we
148 observed that the groups of genomic regions with comparably early maternal replication (Defined in
149 **Fig. 3d** and marked by green squares), were characterized by transcriptional induction in the embryo
150 and high maternally inherited H3K27me3 and H2AUb levels (**Fig. 3j and k**). Conversely, regions with
151 comparably late maternal replication (**Fig. 3d**, purple triangles), were characterized by transcriptional
152 downregulation in the embryo and low maternally inherited H3K27me3 and H2AUb levels (**Fig. 3j and**
153 **k**). Interestingly, the PRC-regulated genomic regions undergoing early replication in the maternal 2-
154 cell genome did not replicate early in ESCs (**Extended Data Fig. 3a, b).** Altogether, this indicates that
155 genome-wide epigenetic diversity across parental genomes is associated with an asynchronous
156 haplotype-specific DNA replication program in the early embryo that is replaced at later stages of
157 embryo development.

158 **Maternal replication timing is associated with nuclear compartmentalization and epigenetic marks**

159 Remarkably, our mapping of replication timing across whole chromosomes uncovered a compelling
160 pattern. Within a 30-megabase (Mb) segment corresponding to the pericentromeric region in the
161 acrocentric mouse autosomes, there was a distinct overabundance of maternally late replicating
162 regions (**Fig. 4a**). In contrast, no such effect was observed within the paternal chromosomes (**Extended**
163 **Data Fig. 5a**). This intriguing observation was consistently observed across individual embryos (**Fig.**
164 **4b**) and was not a characteristic feature in ESCs (**Extended Data Fig. 5b**). The centromeric regions of
165 the chromosomes in 2-cell embryos congregate at one pole of the nucleus near to the nuclear
166 lamina[32]. Therefore, we hypothesized that Lamin-Associated Domains (LADs) might influence the
167 organization of replication timing at the chromosome level. To test this, we utilized recently published
168 genome-wide LAD data from the maternal and paternal haplotypes of 2-cell embryos[33]. Our analysis
169 revealed a strong association between LADs and replication timing in the 2-cell embryos (**Fig. 4c**), and
170 a particularly pronounced enrichment of LADs in the pericentromeric regions (**Fig. 4d**). Interestingly,
171 both parental haplotypes exhibited a pronounced enrichment of LADs in the late replicating regions
172 (**Fig. 4c and e**). However, the distinct partitioning of late replication in the pericentromeric region was
173 exclusively observed in the maternal genome, while no relationship between the paternal
174 pericentromere and late replication was apparent, despite the accumulation of paternal 2-cell LADs
175 in this region (**Fig. 4d and Extended Data Fig. 5a**). Thus, the pericentromeric DNA is organized within

176 LADs of the 2-cell nucleus and asynchronous parental haplotype replication timing is occurring within
177 this domain.

178 To gain a deeper understanding of the coexistence between maternal late replication of LAD-
179 associated regions and our previous observations of histone marks deposited by PRCs enriched in
180 early-replicating maternal regions, we assessed the combined relationship among PRCs-deposited
181 marks, LADs, and replication timing. Interestingly, our findings revealed that among the histone marks
182 deposited by PRCs, H2AUb but more prominently H3K27me3 were most enriched in the part of the
183 genome that do not overlap with LADs (**Fig. 4f**). In contrast, maternal early replication was
184 predominantly partitioned into non-overlapping LAD regions, which also exhibited high enrichment
185 for marks deposited by PRCs, especially H3K27me3 (**Extended Data Fig. 5c-h**). When we analyzed
186 individual loci we found clear late to early replication timing transitions, which overlapped with
187 boundaries between LADs and H3K27me3 (**Fig. 4g**). These results provide the first demonstration of
188 a large-scale asynchronous haplotype-specific replication program that is influenced by higher-order
189 genome organization, such as LADs, transcription, as well as the inheritance of maternal marks
190 deposited by PRCs (**Fig. 4h**).

191 **Discussion**

192 The spatiotemporal pattern of DNA replication has been widely recognized as associated with
193 epigenetic marks, transcriptional activity, and the organization of the 3D genome. Across eukaryotes,
194 a DNA replication program exists, which features constant timing of multi-megabase regions ensuring
195 their replication at specific times during the S phase. These regions are flanked by timing transition
196 regions where DNA replication is progressing[34].

197 In a departure from the norm, our investigation using single Embryo Repli-seq revealed low G1/S
198 deviation in zygotes, which was only partially restored in the 2-Cell embryo compared to mouse
199 embryonic stem cells (ESCs). We propose that this observation suggests an unconventional DNA
200 replication program in the zygote, characterized by the initiation of a high number of replication
201 origins throughout the genome. The partial recovery of the G1/S signal in 2-cell embryos, compared
202 to ESCs, may indicate a gradual establishment of the replication program as embryonic development
203 unfolds. This would be consistent with the embryonic genome activation and the formation of A/B
204 compartments, which are also established gradually during embryogenesis[35,36].

205 Equally fascinating, was the lack of synchrony observed in the 2-cell embryo. Post-translational
206 modifications of histones undergo dynamic changes specific to each parental haplotype following
207 fertilization[37]. We observed a pronounced enrichment of maternally inherited marks deposited by

208 PRCs in the regions that replicate early on the maternal allele. This suggests that the persistence of
209 PRCs-deposited histones from oocytes may play a role in organizing the replication program or be
210 influenced by it.

211 Furthermore, we made intriguing observations regarding the spatial arrangement of DNA replication
212 in the pericentromeric regions of parental chromosomes, which served to further distinguish the
213 events occurring within the parental haplotypes (**Fig. 4g**). We identified consistent late replication in
214 maternal pericentromeric regions in a large fraction of the studied 2-cell embryos and at most
215 chromosomes (**Fig 4a,b, Extended Data Fig. 5a**), which was also characterized by the absence of
216 histone marks deposited by PRCs. One potential explanation for this observation is the spatial
217 separation of parental genomes within the nucleus, which persists until the 8-cell stage[32]. This
218 separation is achieved by congregation of centromeric regions at one pole of the nucleus, while the
219 long chromosome arms and telomeric regions extend towards the opposite pole[32]. This spatial
220 organization plays a pivotal role in establishing the parental-specific nuclear architecture observed
221 during early development. However, the question of why parental haplotypes display such contrasting
222 replication timing in seemingly similar structural domains, such as LADs should be a question for future
223 investigations.

224 Given recent reports of heightened replication stress during the cleavage stages of embryogenesis,
225 the exploration of paternal-specific DNA replication stress and stress-induced DNA breaks across the
226 parental haplotypes becomes a matter of great interest. Moreover, the fragile nature of the
227 pericentromere[38-43] raises intriguing questions about the potential impact of these replication
228 dynamics on the occurrence of gross chromosomal rearrangements, which are relatively common
229 during early embryogenesis[44-46]. Investigations of the role of parental haplotypes in the formation of
230 such rearrangements holds promise for advancing our understanding of embryonic failure and
231 infertility.

232 In summary, our study unveils a notable link between replication timing and genome organization in
233 the early embryo. Specifically, we have discovered a remarkable excess of late replicating regions in
234 the maternal pericentromeric region when compared to paternal chromosomes. The identification of
235 distinct replication timing patterns between maternal and paternal chromosomes emphasizes the
236 intricate nature of replication regulation and its connection to genome organization. The observed
237 association between replication timing, LADs, and maternal histone marks deposited by PRCs reveals
238 an intriguing interplay between epigenetic modifications, nuclear architecture, and replication
239 dynamics.

240

241 **References**

242 1. Hansen, R.S. *et al.* Sequencing newly replicated DNA reveals widespread plasticity in human
243 replication timing. *Proc Natl Acad Sci U S A* **107**, 139-44 (2010).
244 2. Rhind, N. & Gilbert, D.M. DNA replication timing. *Cold Spring Harb Perspect Biol* **5**, a010132
245 (2013).
246 3. Julienne, H., Zoufir, A., Audit, B. & Arneodo, A. Human genome replication proceeds through
247 four chromatin states. *PLoS Comput Biol* **9**, e1003233 (2013).
248 4. Pope, B.D. *et al.* Topologically associating domains are stable units of replication-timing
249 regulation. *Nature* **515**, 402-5 (2014).
250 5. Dileep, V. *et al.* Topologically associating domains and their long-range contacts are
251 established during early G1 coincident with the establishment of the replication-timing
252 program. *Genome Res* **25**, 1104-13 (2015).
253 6. Rivera-Mulia, J.C. *et al.* Dynamic changes in replication timing and gene expression during
254 lineage specification of human pluripotent stem cells. *Genome Res* **25**, 1091-103 (2015).
255 7. Aran, D., Toperoff, G., Rosenberg, M. & Hellman, A. Replication timing-related and gene body-
256 specific methylation of active human genes. *Hum Mol Genet* **20**, 670-80 (2011).
257 8. Suzuki, M. *et al.* Late-replicating heterochromatin is characterized by decreased cytosine
258 methylation in the human genome. *Genome Res* **21**, 1833-40 (2011).
259 9. Dileep, V. & Gilbert, D.M. Single-cell replication profiling to measure stochastic variation in
260 mammalian replication timing. *Nat Commun* **9**, 427 (2018).
261 10. Miura, H. *et al.* Single-cell DNA replication profiling identifies spatiotemporal developmental
262 dynamics of chromosome organization. *Nat Genet* **51**, 1356-1368 (2019).
263 11. Marchal, C. *et al.* Genome-wide analysis of replication timing by next-generation sequencing
264 with E/L Repli-seq. *Nat Protoc* **13**, 819-839 (2018).
265 12. Dahl, J.A. *et al.* Broad histone H3K4me3 domains in mouse oocytes modulate maternal-to-
266 zygotic transition. *Nature* **537**, 548-552 (2016).
267 13. Liu, X. *et al.* Distinct features of H3K4me3 and H3K27me3 chromatin domains in pre-
268 implantation embryos. *Nature* **537**, 558-562 (2016).
269 14. Zhang, B. *et al.* Allelic reprogramming of the histone modification H3K4me3 in early
270 mammalian development. *Nature* **537**, 553-557 (2016).
271 15. Xia, W. *et al.* Resetting histone modifications during human parental-to-zygotic transition.
272 *Science* **365**, 353-360 (2019).
273 16. Chen, Z., Djekidel, M.N. & Zhang, Y. Distinct dynamics and functions of H2AK119ub1 and
274 H3K27me3 in mouse preimplantation embryos. *Nat Genet* **53**, 551-563 (2021).
275 17. Peaston, A.E. *et al.* Retrotransposons regulate host genes in mouse oocytes and
276 preimplantation embryos. *Dev Cell* **7**, 597-606 (2004).
277 18. Franke, V. *et al.* Long terminal repeats power evolution of genes and gene expression
278 programs in mammalian oocytes and zygotes. *Genome Res* **27**, 1384-1394 (2017).
279 19. Sankar, A. *et al.* KDM4A regulates the maternal-to-zygotic transition by protecting broad
280 H3K4me3 domains from H3K9me3 invasion in oocytes. *Nat Cell Biol* **22**, 380-388 (2020).
281 20. Brind'Amour, J. *et al.* LTR retrotransposons transcribed in oocytes drive species-specific and
282 heritable changes in DNA methylation. *Nat Commun* **9**, 3331 (2018).
283 21. McLay, D.W. & Clarke, H.J. Remodelling the paternal chromatin at fertilization in mammals.
284 *Reproduction* **125**, 625-33 (2003).
285 22. Aguirre-Lavin, T. *et al.* 3D-FISH analysis of embryonic nuclei in mouse highlights several abrupt
286 changes of nuclear organization during preimplantation development. *BMC Dev Biol* **12**, 30
287 (2012).
288 23. Palmerola, K.L. *et al.* Replication stress impairs chromosome segregation and preimplantation
289 development in human embryos. *Cell* **185**, 2988-3007 e20 (2022).

290 24. Kort, D.H. *et al.* Human embryos commonly form abnormal nuclei during development: a
291 mechanism of DNA damage, embryonic aneuploidy, and developmental arrest. *Hum Reprod*
292 **31**, 312-23 (2016).
293 25. Moindrot, B. *et al.* 3D chromatin conformation correlates with replication timing and is
294 conserved in resting cells. *Nucleic Acids Res* **40**, 9470-81 (2012).
295 26. Sima, J. *et al.* Identifying cis Elements for Spatiotemporal Control of Mammalian DNA
296 Replication. *Cell* **176**, 816-830 e18 (2019).
297 27. Muller, C.A. & Nieduszynski, C.A. DNA replication timing influences gene expression level. *J*
298 *Cell Biol* **216**, 1907-1914 (2017).
299 28. Mei, H. *et al.* H2AK119ub1 guides maternal inheritance and zygotic deposition of H3K27me3
300 in mouse embryos. *Nat Genet* **53**, 539-550 (2021).
301 29. Xu, Q. *et al.* SETD2 regulates the maternal epigenome, genomic imprinting and embryonic
302 development. *Nat Genet* **51**, 844-856 (2019).
303 30. Ishiuchi, T. *et al.* Reprogramming of the histone H3.3 landscape in the early mouse embryo.
304 *Nat Struct Mol Biol* **28**, 38-49 (2021).
305 31. Zhang, C. *et al.* The chromatin remodeler Snf2h is essential for oocyte meiotic cell cycle
306 progression. *Genes Dev* **34**, 166-178 (2020).
307 32. Mayer, W., Smith, A., Fundele, R. & Haaf, T. Spatial separation of parental genomes in
308 preimplantation mouse embryos. *J Cell Biol* **148**, 629-34 (2000).
309 33. Borsos, M. *et al.* Genome-lamina interactions are established de novo in the early mouse
310 embryo. *Nature* **569**, 729-733 (2019).
311 34. Marchal, C., Sima, J. & Gilbert, D.M. Control of DNA replication timing in the 3D genome. *Nat*
312 *Rev Mol Cell Biol* **20**, 721-737 (2019).
313 35. Ke, Y. *et al.* 3D Chromatin Structures of Mature Gametes and Structural Reprogramming
314 during Mammalian Embryogenesis. *Cell* **170**, 367-381 e20 (2017).
315 36. Du, Z. *et al.* Allelic reprogramming of 3D chromatin architecture during early mammalian
316 development. *Nature* **547**, 232-235 (2017).
317 37. Zheng, H. *et al.* Resetting Epigenetic Memory by Reprogramming of Histone Modifications in
318 Mammals. *Mol Cell* **63**, 1066-79 (2016).
319 38. Wolff, D.J., Miller, A.P., Van Dyke, D.L., Schwartz, S. & Willard, H.F. Molecular definition of
320 breakpoints associated with human Xq isochromosomes: implications for mechanisms of
321 formation. *Am J Hum Genet* **58**, 154-60 (1996).
322 39. Barbouti, A. *et al.* The breakpoint region of the most common isochromosome, i(17q), in
323 human neoplasia is characterized by a complex genomic architecture with large, palindromic,
324 low-copy repeats. *Am J Hum Genet* **74**, 1-10 (2004).
325 40. Scott, S.A., Cohen, N., Brandt, T., Warburton, P.E. & Edelmann, L. Large inverted repeats within
326 Xp11.2 are present at the breakpoints of isodicentric X chromosomes in Turner syndrome.
327 *Hum Mol Genet* **19**, 3383-93 (2010).
328 41. Costa, G., Barra, V., Lentini, L., Cilluffo, D. & Di Leonardo, A. DNA demethylation caused by 5-
329 Aza-2'-deoxycytidine induces mitotic alterations and aneuploidy. *Oncotarget* **7**, 3726-39
330 (2016).
331 42. Martinez, A.C. & van Wely, K.H. Centromere fission, not telomere erosion, triggers
332 chromosomal instability in human carcinomas. *Carcinogenesis* **32**, 796-803 (2011).
333 43. Gravholt, C.H., Friedrich, U., Caprani, M. & Jorgensen, A.L. Breakpoints in Robertsonian
334 translocations are localized to satellite III DNA by fluorescence in situ hybridization. *Genomics*
335 **14**, 924-30 (1992).
336 44. Girardi, G., Lingo, J.J., Fleming, S.D. & Regal, J.F. Essential Role of Complement in Pregnancy:
337 From Implantation to Parturition and Beyond. *Front Immunol* **11**, 1681 (2020).
338 45. Escriba, M.J., Vendrell, X. & Peinado, V. Segmental aneuploidy in human blastocysts: a
339 qualitative and quantitative overview. *Reprod Biol Endocrinol* **17**, 76 (2019).

340 46. Babariya, D., Fragouli, E., Alfarawati, S., Spath, K. & Wells, D. The incidence and origin of
341 segmental aneuploidy in human oocytes and preimplantation embryos. *Hum Reprod* **32**, 2549-
342 2560 (2017).

343

344 **Online methods**

345 **mESC Cell Culture**

346 F121-9 mESC line (RRID: CVCL_VC42, a gift from Joost Gribnau) was cultured on 6-well plates
347 previously coated with 0.01% poly-l-ornithine (Sigma P3655) for 1 hour. Subsequently, the plates were
348 further coated with 300pg/ml of laminin (Fisher Scientific 10152421) for a minimum of 1 hour.

349 The mESCs were maintained in 2i and LIF media as previously described[47], which was refreshed every
350 24 hours to ensure optimal growth and viability.

351 **Sample preparation for single cell RT profiling of mESC cells**

352 Sample preparation of mouse ESCs for single-cell Repliseq was performed following previously
353 established protocols[48,49]. In brief, detached single cells were resuspended in 1 ml of 1% fetal bovine
354 serum (FBS) in phosphate-buffered saline (PBS). Subsequently, the cells were fixed by slowly adding 3
355 ml of ice-cold 100% ethanol and incubating the mixture at -20°C for 30 minutes.

356 To ensure accurate cell cycle phase identification, $1x10^6$ cells were washed and resuspended in 700 µl
357 of propidium iodide (PI) staining solution. The PI staining solution comprised of 350 µl of 1 mg/ml PI,
358 70 µl of 10 mg/ml RNase A, and 7 ml of 1% FBS-PBS.

359 Flow cytometric sorting was performed using a Sony SH800 sorter to isolate single cells in the G1 or S
360 phase, based on their PI staining profile. The sorted single cells were collected directly into individual
361 wells of a 96-well plate. Each well contained 6 µl of single-cell lysis and fragmentation buffer,
362 comprising of 3 µl of proteinase K, 50 µl of 10x Single Cell Lysis and Fragmentation Buffer (Sigma;
363 L1043), and 447 µl of autoclaved double-distilled water (ddH2O).

364 Following collection, the plate was briefly centrifuged and subsequently stored at -80°C until further
365 processing for single-cell sequencing.

366 **Spermatozoa cryopreservation**

367 For cryopreservation of mouse sperm, a modified version of a previously established protocol was
368 utilized[50].

369 In brief, ten 0.25 mL clear plastic straws (Minitube GmbH; 13407/0010) were labeled for each
370 individual mouse. A proven fertile male mouse, aged between 3 to 8 months, was sacrificed following
371 one week of solitary housing. The cauda epididymis and vas deferens were dissected and placed in 1
372 mL of Dulbecco's phosphate-buffered saline (DPBS). Under a dissection microscope, adipose and
373 vascular tissues were carefully removed. Both cauda epididymides were then transferred to a 35mm

374 dish containing a 120 µl droplet of gCPA sperm cryopreservation media (in-house) covered with NidOil
375 (Nidacon; NO-100).

376 Using a pair of watchmaker scissors, the epididymides were cut several times to release the sperm
377 and facilitate its separation from the tissue. The dish was placed in a CO2 incubator at 37°C with 5%
378 CO2. To aid sperm dispersion and release, the dish was gently swirled once every minute for a total of
379 3 minutes.

380 Ten 10 µl aliquots of the sperm suspension were taken from the dish and deposited onto the lid of a
381 35mm culture dish. Clear plastic straws were prepared for freezing by drawing up HTF medium
382 (developed in-house) into the straw using a syringe, followed by a small amount of air, and then the
383 10 µl aliquot of sperm. Additional air was introduced into the straw before sealing it with a metal ball
384 (Minitube GmbH; 13400/9970).

385 All ten straws were then placed in the gaseous phase of liquid nitrogen for a duration of 10 minutes.
386 Subsequently, the straws were slowly and carefully immersed into the liquid phase of nitrogen before
387 being transferred to a -150°C freezer or long-term liquid nitrogen storage for preservation.

388 ***In Vitro* fertilization of mouse oocytes**

389 *In vitro* fertilization of mouse oocytes was performed as previously described but with some
390 modifications[50]. Briefly, a single straw of cryopreserved sperm from CAST/EiJ mice was thawed for 10
391 minutes in a water bath set to 37°C. After thawing, the sperm was dispersed into 90 µl of TYH+MBCD
392 (in house) sperm pre-incubation medium in a 35mm dish coated with NidOil (Nidacon; NO-100). The
393 dish was equilibrated at 37°C for 20 minutes in a 5% CO_2 in air environment.

394 Simultaneously, a 30mm fertilization dish was prepared by adding 90 µl droplet of 2 mM reduced
395 glutathione (Sigma, G4251) in HTF (in house) and covering it with NidOil. The dish was equilibrated for
396 at least 30 minutes at 37°C in a 5% CO2 in air environment.

397 Female C57/BL6N mice were superovulated by intraperitoneal injection of 7.5 IU of hCG (Sigma; CG5)
398 and 7.5 IU of PMSG (Prospec; HOR-272) 48 hours later. After 15 hours from the second injection, the
399 mice were euthanized, and the oviducts were dissected and placed into the warm NidOil of the
400 fertilization dish. Cumulus-enclosed oocytes were transferred from the ampoule into the fertilization
401 droplet.

402 Following a 30-minute pre-incubation, 10 µl of the most motile sperm was extracted from the pre-
403 incubation droplet and added to the fertilization dish containing the cumulus-enclosed oocytes. The
404 dish was then incubated for three hours.

405 Meanwhile, a wash dish was prepared by creating four droplets of 90 µl of Advanced KSOM embryo
406 media (Sigma; MR-101) in a 60mm dish. The dish was covered with NidOil and equilibrated for 30
407 minutes at 37°C in a 5% CO2 environment.

408 Subsequently, the fertilized oocytes were washed through the four wash droplets to remove the
409 cumulus cells and sperm. The oocytes were then incubated until they were ready for Single-Embryo
410 Repli-Seq.

411 **EdU labelling of single mouse embryos**

412 To determine the duration of the first and second S phase, we conducted pulse labeling of single 2-
413 cell stage embryos using the Click-iT EdU Cell Proliferation Kit for Imaging (ThermoFisher Scientific;
414 C10340). The incorporation of EdU was assessed through microscopy. The experimental procedure
415 was as follows:

416 Embryos were obtained at the zygote (no prior treatment) or the 2-cell stage following release from
417 Nocodazole synchronization. At hourly intervals, individual zygotes or 2-cell embryos were transferred
418 to pre-equilibrated droplets of Advanced KSOM embryo media (Sigma; MR-101) containing 500 µM
419 EdU. The droplets were maintained at 37°C in a 5% CO2 environment. After a 30-minute incubation
420 period, the embryos were washed with Advanced KSOM media and fixed in 4% paraformaldehyde
421 (PFA) for 15 minutes at room temperature. Subsequently, the embryos were transferred to a wash
422 buffer consisting of 5% BSA in PBS and incubated on a rocking stage at 4°C for 48 hours. To
423 permeabilize the embryos, they were treated with 0.5% Triton X-100 in PBS for 20 minutes at room
424 temperature, followed by rinsing in PBST (0.1% Tween 20 in PBS) for 20 minutes at room temperature.
425 The embryos were then subjected to the Click-iT EdU cell proliferation reaction cocktail, according to
426 the manufacturer's instructions. They were incubated in the reaction cocktail for 1 hour. After the
427 incubation, the embryos were rinsed in a wash buffer containing 20 µg/ml DAPI (ThermoFisher
428 Scientific; D1306) for 30 minutes.

429 For imaging, embryos from the same time point were mounted using SlowFade Diamond Antifade
430 Mountant (ThermoFisher Scientific; S36967) between two No.1 coverslip. Confocal microscopy
431 imaging was performed using an LSM900 confocal laser scanning microscope (Zeiss) equipped with a
432 40x Plan-Apochromat objective. The Alexa 647 fluorophore was excited using a 639-nm laser, and
433 DAPI was excited using a 405-nm laser. Image processing was performed using Zen software and
434 ImageJ[51] software for quantification of corrected total fluorescence.

435 **Sample preparation for RT profiling of single mouse embryos (Single-Embryo Repli-Seq)**

436 Zygotes collected after IVF were categorized into G1 or S phase. G1 phase was determined by two
437 pronuclei detection, while S phase was determined by timing established using prior EdU
438 incorporation experiments. Zona pellucida and polar bodies were removed using a dissection
439 microscope, and naked zygotes were transferred to a low-adhesion 96-well PCR plate. Each well
440 contained 6 µl of single-cell lysis and fragmentation buffer (3 µl proteinase K, 50 µl 10x Single Cell Lysis
441 and Fragmentation Buffer (Sigma; L1043), and 447 µl ddH2O). The plate was centrifuged and stored
442 at -80°C for single-cell sequencing.

443 For 2-cell embryos, fifteen hours after combining sperm with cumulus-enclosed oocytes, the resulting
444 zygotes were transferred using a mouth pipette into a 90 µl droplet of Advanced KSOM embryo media
445 (Sigma; MR-101) containing 40 nM Nocodazole. The droplet was placed in a 30mm dish covered with
446 NidOil (Nidacon; NO-100). This step synchronized the zygotes in the G2/M phase from which they
447 were released after 4 hours.

448 Following the synchronization period, the zygotes were washed through seven droplets of Advanced
449 KSOM embryo media, each covered with NidOil. These droplets were pre-equilibrated for 30 minutes
450 at 37°C in a 5% CO2 environment.

451 Under normal circumstances, the zygotes divide within 1 hour after release from the block. At this
452 point, G1 phase 2-cell stage embryos were promptly processed by removing the zona pellucida and
453 polar bodies (if present) using a dissection microscope. The resulting naked embryos were then
454 transferred to a low-adhesion 96-well PCR plate. Each well contained 6 µl of single-cell lysis and
455 fragmentation buffer. The plate was briefly centrifuged and subsequently stored at -80°C until
456 preparation for single-cell sequencing.

457 For the processing of single S-phase embryos, the same procedure was followed. However, accurate
458 selection of S-phase embryos was based on prior EdU labeling experiments, which determined the
459 time of entry and exit from the S phase after release from Nocodazole synchronization. Specifically,
460 early S-phase cells were selected 3 hours after release, mid-S-phase cells were selected 5 hours after
461 release, and late-S-phase cells were selected 6 hours after release.

462 **Sample preparation and sequencing for single embryo RT profiling**

463 After sample preparation, single embryos or single mouse embryonic stem cells (mESCs) were
464 processed for single-cell sequencing following a previously published single-cell Reli-Seq protocol[48,49].
465 After whole-genome amplification, the samples were quantified using the Qubit dsDNA HS assay kit
466 (ThermoFisher; Q32851). The quantification of the samples was further confirmed by checking the
467 product size using the Agilent Tapestation 2200 High Sensitivity system (Agilent; 5067). For library

468 preparation, we utilized the KAPA Hyper Prep Library Preparation Kit (Roche; KK8502) in combination
469 with IDT for Illumina TruSeq DNA UD Indexes (Illumina; 20023784). The end repair and A-tailing steps
470 were performed using 40 ng of whole-genome amplified DNA. The reaction volume was scaled down
471 to 1/5th of the recommended reaction volume and vortexed and briefly spun down before incubating
472 on a thermocycler at 20°C for 30 minutes, followed by 65°C for 30 minutes, and then held at 4°C.
473 Adaptor ligation was performed in the same plate as the end repair and A-tailing reaction. The reaction
474 mixture consisted of 12 µl end repair and A-tailing reaction product, 0.5 µl IDT for Illumina TruSeq DNA
475 UD Indexes, 1.5 µl PCR-grade water, 6 µl ligation buffer, and 2 µl DNA ligase. The reaction mixture was
476 vortexed, spun down, and incubated at 20°C for 15 minutes. Post-adaptor ligation cleanup was
477 performed using 0.8X Agencourt AMPure XP beads (Beckman Coulter; A63881), following the
478 instructions provided with the KAPA Hyper Prep Kit. Library amplification was carried out by scaling
479 down the recommended manufacturer's protocol to 1/5th and using 11 µl of the bead-cleaned post-
480 ligation product. Amplification was performed using a thermocycler with an initial denaturation step
481 of 98°C for 45 seconds, followed by 5 PCR cycles at 98°C for 15 seconds, 60°C for 30 seconds, and 72°C
482 for 30 seconds. After the final cycle, an extension step was included, and the samples were incubated
483 at 72°C for 1 minute, followed by holding at 4°C. The samples were then cleaned according to the
484 KAPA Hyper Prep Kit post-amplification cleanup instructions using 0.9X Agencourt AMPure XP beads.
485 The final libraries were quantified using the Qubit dsDNA HS kit and assessed for library size using the
486 Agilent Tapestation 2200 High Sensitivity system. The libraries were sequenced on a NextSeq550
487 platform using a 150-bp single-end read format.

488 **Single-Embryo and single mESC Repli-Seq data analysis**

489 Our single embryo Repli-Seq data analysis, which was used to analyse all embryos and single mESCs,
490 was based on two previously published protocols[48,49,52]. We followed the analysis pipeline described
491 by Miura et al. (2019) and Miura et al. (2020) up to the generation of log2 fold replication timing (RT)
492 scores, with some modifications. The binarization of Replication Status followed the piecewise copy
493 fit and mixture modelling approach outlined by Dileep and Gilbert (2018) with adaptations for our
494 analysis. This relied on the R-packages Zoo, Fbasics, Mixtools, and Copynumber[53].

495 Fastq files for G1 and S phase were checked for quality using FastQC[54,55] and trimmed for Illumina
496 index and Seqplex adaptor sequences using Cutadapt[56], as described in previous studies[48,49]. For
497 haplotype analysis, sequencing reads were mapped to a modified mm10 reference genome that
498 included N-masked positions for single hybrid strains. The N masked genome was created using the
499 genome preparation command of the SNPsplit package[57], which incorporates N-masking into the
500 mm10 reference for the CAST/EiJ genome from the Mouse genome project V7 vcf file[58-60].

501 Subsequently, this new mm10 N-masked genome was then used to map the trimmed sequencing
502 reads using bowtie2[61] for parsed haplotype analysis, alternatively unparsed haplotype analysis was
503 performed using the original mm10 reference genome and duplicate reads were marked with Picard
504 (http://broadinstitute.github.io/picard).

505 To divide the reads into maternal and paternal haplotypes, we used the allele-specific alignment sorter
506 SNPsplit[57], which utilized a list of known SNP positions between C57BL/6 and CAST/EiJ mice. Quality
507 control of parsed BAM files was confirmed using SAMStat[62,63], and typically, we obtained >50% reads
508 with >30 MAPQ. To calculate log2 fold replication timing scores, a G1 reference file was generated
509 from more than three G1 control cells with a normal karyotype. The karyotype was confirmed using
510 the hidden Markov model of the findCNVs command in the Aneufinder package[64], as previously
511 described[48,49]. In our analysis of mESC, we made the decision to exclude chromosome 3 and
512 chromosome 8 due to aneuploidy.

513 Computing of RT scores were performed by counting reads in sliding windows of 200 kb at 40 kb
514 intervals normalized to the G1 control according to the standard scRepliseq analysis or haplotype
515 resolved scRepliseq analysis previously published protocol for unphased and phased haplotype
516 analysis, respectively[49]. Log2 fold RT scores were converted to binary RT scores using a previously
517 outlined protocol, with binary values determined using the skew approach when the component
518 means from the mixture modelling were <0.25[52].

519 The Replication Score for each sample was obtained by calculating the fraction of the genome that
520 had been replicated based on the binary scores for each sample, ignoring bins from masked parts of
521 the genome. A matrix assembly was generated containing Normalized Repli-seq enrichment and
522 binarized Replication Status for each cell. Data aggregation for this was done using the merge
523 command in R (v. 4.1.2)[65] and IDs for each bin consisting of chromosome name and start coordinate
524 for all datasets. This was performed separately for three pairwise comparisons, published vs. our ESC
525 data, ESC vs. 2-cell data, and maternal vs. paternal 2-cell data, resulting in output that only included
526 the relevant datasets and covered parts of the genome where data were present in all input samples
527 (**Supplementary Tables 1,4,6**). Subsequent analysis was performed in EaSeq (see below)[66] after
528 importing bedgraphs-files of log2-fold enrichment comparisons between S-phase and G1-phase
529 samples as well as bedgraphs of Binarized Replication Status as 'datasets'.

530 **Genomic data sources and quality control**

531 Previously published Repli-seq data from single ESCs[52] were downloaded from the NCBI GEO
532 database[67], accession GSE102077. Lamin-associated domains in maternal and paternal 2-cell embryos

533 were identified in[68] and bed-files with allele-specific coordinates were downloaded from the NCBI GEO
534 database[67], accession GSE112551. Refseq genome annotations[69] for mm10 were downloaded from
535 the UCSC table browser[70]. Read qualities were analyzed using FastQC[55], fastqScreen (v. 0.11.4)[71], and
536 MultiQC (v. 1.7)[72].

537 **ChIP-seq, Cut&Run, RNA-seq, and ATAC-seq data sourcing and processing**

538 ChIP-seq of histone marks and corresponding input from MII oocytes were published in[73-77], Cut&Run
539 of the histone variant H3.3 in MII oocytes published in[78], and ATAC-seq from fully grown oocytes
540 published[79]. A complete list can be found in **Supplementary Table 3**. Single oocyte / embryo RNA-seq
541 was previously published[77] and was processed as described in[80]. ChIP-seq, Cut&Run, and ATAC-seq
542 reads were analyzed using FastQC and trimmed using Trimgalore[81]. Reads were mapped using
543 bowtie2[61], and handled using Samtools[82]. Blacklisted regions[83] were obtained from
544 https://github.com/Boyle-Lab/Blacklist/archive/v2.0.zip and removed using bedtools intersect -v[84].
545 Subsequent analysis was performed in EaSeq (see below)[66] after importing mapped reads from Bam-
546 files as 'datasets'. For ChIP-seq, Cut&Run and ATAC-seq this was done using default settings, including
547 deduplication. For RNA-seq removal of duplicates was disabled.

548 **Repli-seq analysis and visualization**

549 Analysis and visualization was done using EaSeq (v. 1.12)[66], Microsoft Excel 2016 for simple bar
550 diagrams and line charts, and R (v. 4.1.2)[65] for Boxplots and interquartile range plots as well as the
551 beeswarm package (v.0.4.0, https://github.com/aroneklund/beeswarm) for Bee-swarm plots. In
552 EaSeq, Genome browser tracks and annotations were made using the EaSeq plot tools 'FillTrack',
553 'Annot.' and 'RegionMap' for LADs (available in the beta-testing panel). Scatter plots and heatmaps of
554 ChIP-seq, Cut&Run, ATAC-seq, and RNA-seq values were made using the EaSeq tools 'Scatter' and
555 'ParMap'. Assembled matrices (**Supplementary Tables 4-6**) and LAD coordinates we imported as
556 'Regionsets' in EaSeq. Heatmaps of single-embryo log2-fold enrichment comparisons between S-
557 phase and G1-phase samples as well as heatmaps of Binarized Replication Status at individual loci (as
558 well as averages from multiple loci) were generated using the 'Multi Track' tool available in the 'Beta-
559 testing' panel of EaSeq. ChIP-seq, Cut&Run, and ATAC-seq Signal intensities at the bins in the matrix
560 assemblies were quantified using the EaSeq tool 'Quantify', using default normalization (Fragments
561 Per Kilobase per Million reads – FPKM) for scatter plots and clustered heatmaps. Similarly, RNA-seq
562 read densities were quantified using the EaSeq tool 'Quantify' but with normalization disabled to
563 obtain matrices of raw read counts. Following this, a pseudoread was added to RNA-seq read counts,
564 and all quantified RNA-seq counts in a matrix assembly were quantile normalized using the tool
565 'Normalize'. These normalized values were used to calculate means for each condition as well as log2

566 fold difference from the mean using the EaSeq tool 'Calculate'. Heatmaps of feature density e.g. ChIP-
567 seq, RNA-seq signal, or LAD-overlap were generated using the tool 'Z-scatter'. Similarly, plots of
568 features at autosomes were generated using this tool and the autosome number for the Y-axis and
569 start coordinate of each bin for the X-axis. Overlap with LADs for each matrix assembly was
570 determined using the EaSeq tool 'Coloc'. Subpopulations were obtained using the 'Gate' tool.

571 **Repliseq clustering**

572 Hierarchical clustering was performed in R (v. 4.1.2)[65] on scaled and transformed (R-commands: scale()
573 and t(), default settings) log2-fold Repli-seq enrichment using the command dist(method = 'euclidean')
574 to calculate a distance matrix, and a dendrogram was plotted after hierarchically clustering the
575 distance matrix using the command hclust(method = 'ward.D2'). k-means-clustering was performed
576 in EaSeq, using the tool 'ClusterP with all additional normalization disabled. Clustering was performed
577 individually for comparisons between 2-cell and ESC data and 2-cell maternal and paternal data.

578 **Statistics**

579 All statistics was performed as described in legends using R (v. 4.1.2)[65].

580 **Code availability**

581 Scripts for diploid and haplotype-resolved Repli-seq processing were acquired from
582 https://github.com/kuzobuta/scRepliseq-Pipeline and https://github.com/kuzobuta/scRepliseq-
583 Pipeline/tree/master/scripts/haplotype-resolved-analysis. EaSeq and source code is available at
584 http://easeq.net

585 **Data availability**

586 **------ FOR REVIEWERS (will be deleted from the manuscript upon acceptance): ------**

587 **To review GEO accession GSE237400 (First submission data):**

588 Reviewer access to the unpublished Repli-seq data for the first submission of this study can be
589 obtained using the link https://www.ncbi.nlm.nih.gov/geo/query/acc.cgi?acc=GSE237400 and by
590 entering the token abyfqaiwjrwnrob into the box.

591 **----------**

592 The Repli-seq data generated for this publication have been deposited in NCBI's Gene Expression
593 Omnibus[67] and are accessible through GEO Series accession number GSE237400
594 (https://www.ncbi.nlm.nih.gov/geo/query/acc.cgi?acc=GSE237400).

595

596 47. Hayashi, K. & Saitou, M. Generation of eggs from mouse embryonic stem cells and induced
597 pluripotent stem cells. *Nat Protoc* **8**, 1513-24 (2013).
598 48. Miura, H. *et al.* Single-cell DNA replication profiling identifies spatiotemporal developmental
599 dynamics of chromosome organization. *Nat Genet* **51**, 1356-1368 (2019).
600 49. Miura, H. *et al.* Mapping replication timing domains genome wide in single mammalian cells
601 with single-cell DNA replication sequencing. *Nat Protoc* **15**, 4058-4100 (2020).
602 50. Nakagata, N. Cryopreservation of Mouse Spermatozoa and In Vitro Fertilization. in *Transgenic*
603 *Mouse Methods and Protocols* (eds. Hofker, M.H. & van Deursen, J.) 57-73 (Humana Press,
604 Totowa, NJ, 2011).
605 51. Schindelin, J. *et al.* Fiji: an open-source platform for biological-image analysis. *Nat Methods* **9**,
606 676-82 (2012).
607 52. Dileep, V. & Gilbert, D.M. Single-cell replication profiling to measure stochastic variation in
608 mammalian replication timing. *Nat Commun* **9**, 427 (2018).
609 53. Nilsen, G. *et al.* Copynumber: Efficient algorithms for single- and multi-track copy number
610 segmentation. *BMC Genomics* **13**, 591 (2012).
611 54. FastQC https://qubeshub.org/resources/fastqc. (2015).
612 55. Andrews, S. FastQC: A Quality Control Tool for High Throughput Sequence Data. Available at:
613 http://www.bioinformatics.babraham.ac.uk/projects/fastqc/. (2010).
614 56. Martin, M. Cutadapt removes adapter sequences from high-throughput sequencing reads.
615 *EMBnet.journal; Vol 17, No 1: Next Generation Sequencing Data AnalysisDO -*
616 *10.14806/ej.17.1.200* (2011).
617 57. Krueger, F. & Andrews, S.R. SNPsplit: Allele-specific splitting of alignments between genomes
618 with known SNP genotypes. *F1000Res* **5**, 1479 (2016).
619 58. Keane, T.M. *et al.* Mouse genomic variation and its effect on phenotypes and gene regulation.
620 *Nature* **477**, 289-94 (2011).
621 59. Doran, A.G. *et al.* Deep genome sequencing and variation analysis of 13 inbred mouse strains
622 defines candidate phenotypic alleles, private variation and homozygous truncating mutations.
623 *Genome Biol* **17**, 167 (2016).
624 60. Lilue, J. *et al.* Sixteen diverse laboratory mouse reference genomes define strain-specific
625 haplotypes and novel functional loci. *Nat Genet* **50**, 1574-1583 (2018).
626 61. Langmead, B. & Salzberg, S.L. Fast gapped-read alignment with Bowtie 2. *Nat Methods* **9**, 357-
627 9 (2012).
628 62. Lassmann, T. SAMStat 2: quality control for next generation sequencing data. *Bioinformatics*
629 **39**(2023).
630 63. Lassmann, T., Hayashizaki, Y. & Daub, C.O. SAMStat: monitoring biases in next generation
631 sequencing data. *Bioinformatics* **27**, 130-1 (2011).
632 64. Bakker, B. *et al.* Single-cell sequencing reveals karyotype heterogeneity in murine and human
633 malignancies. *Genome Biol* **17**, 115 (2016).
634 65. R Core Team R: A language and environment for statistical computing. R Foundation for
635 Statistical Computing, Vienna, Austria. (2021).
636 66. Lerdrup, M., Johansen, J.V., Agrawal-Singh, S. & Hansen, K. An interactive environment for
637 agile analysis and visualization of ChIP-sequencing data. *Nat Struct Mol Biol* **23**, 349-57 (2016).
638 67. Edgar, R., Domrachev, M. & Lash, A.E. Gene Expression Omnibus: NCBI gene expression and
639 hybridization array data repository. *Nucleic Acids Res* **30**, 207-10 (2002).
640 68. Borsos, M. *et al.* Genome-lamina interactions are established de novo in the early mouse
641 embryo. *Nature* **569**, 729-733 (2019).
642 69. O'Leary, N.A. *et al.* Reference sequence (RefSeq) database at NCBI: current status, taxonomic
643 expansion, and functional annotation. *Nucleic Acids Res* **44**, D733-45 (2016).
644 70. Karolchik, D. *et al.* The UCSC Table Browser data retrieval tool. *Nucleic Acids Res* **32**, D493-6
645 (2004).

646 71. Wingett, S.W. & Andrews, S. FastQ Screen: A tool for multi-genome mapping and quality
647 control. *F1000Res* **7**, 1338 (2018).
648 72. Ewels, P., Magnusson, M., Lundin, S. & Kaller, M. MultiQC: summarize analysis results for
649 multiple tools and samples in a single report. *Bioinformatics* **32**, 3047-8 (2016).
650 73. Chen, Z., Djekidel, M.N. & Zhang, Y. Distinct dynamics and functions of H2AK119ub1 and
651 H3K27me3 in mouse preimplantation embryos. *Nat Genet* **53**, 551-563 (2021).
652 74. Dahl, J.A. *et al.* Broad histone H3K4me3 domains in mouse oocytes modulate maternal-to-
653 zygotic transition. *Nature* **537**, 548-552 (2016).
654 75. Liu, X. *et al.* Distinct features of H3K4me3 and H3K27me3 chromatin domains in pre-
655 implantation embryos. *Nature* **537**, 558-562 (2016).
656 76. Xu, Q. *et al.* SETD2 regulates the maternal epigenome, genomic imprinting and embryonic
657 development. *Nat Genet* **51**, 844-856 (2019).
658 77. Sankar, A. *et al.* KDM4A regulates the maternal-to-zygotic transition by protecting broad
659 H3K4me3 domains from H3K9me3 invasion in oocytes. *Nat Cell Biol* **22**, 380-388 (2020).
660 78. Ishiuchi, T. *et al.* Reprogramming of the histone H3.3 landscape in the early mouse embryo.
661 *Nat Struct Mol Biol* **28**, 38-49 (2021).
662 79. Zhang, C. *et al.* The chromatin remodeler Snf2h is essential for oocyte meiotic cell cycle
663 progression. *Genes Dev* **34**, 166-178 (2020).
664 80. Sankar, A., Johansen, J. V., Borup, R. Single oocyte/embryo RNASeq data processing.
665 *Protocolexchange* (2020).
666 81. Felix Krueger, F.J., Phil Ewels, Ebrahim Afyounian, & Benjamin Schuster-Boeckler. (2021).
667 82. Li, H. *et al.* The Sequence Alignment/Map format and SAMtools. *Bioinformatics* **25**, 2078-9
668 (2009).
669 83. Amemiya, H.M., Kundaje, A. & Boyle, A.P. The ENCODE Blacklist: Identification of Problematic
670 Regions of the Genome. *Sci Rep* **9**, 9354 (2019).
671 84. Quinlan, A.R. & Hall, I.M. BEDTools: a flexible suite of utilities for comparing genomic features.
672 *Bioinformatics* **26**, 841-2 (2010).

673

674 **Acknowledgements**

675 We thank the members of the Hoffmann lab and Center for Chromosome Stability for support and
676 critical suggestions throughout this work. We thank Ricardo Alonso Laguna Barraza, Rodrigo Dos A
677 Garcia and Ioana Maria Zah of the Core Facility of Transgenic Mice, The University of Copenhagen for
678 their technical support. We acknowledge the Core Facility for Integrated Microscopy, Faculty of Health
679 and Medical Sciences, University of Copenhagen.

680

681 **Funding**

682 This work was supported by the Danish National Research Foundation (grant DNRF115). J.A.H. is
683 funded by a postdoctoral fellowship award by the Lundbeck Foundation (R347-2020-2177). Research
684 in the E.R.H. lab is funded by the ERC (724718-ReCAP), Novo Nordisk Foundation
685 (NNF15COC0016662), a project grant from the DFF-FSS (0134-00299B) and Danish National Research
686 Foundation Center (6110-00344B).

687

688 **Author contributions**

689 J.A.H., E.R.H. and M.L. conceived the study and designed experiments. J.A.H. and J.M.G. planned and
690 handled mouse work, IVF, and embryo collection. Embryo culture, labeling, imaging, and experiments
691 was carried out by J.A.H. Library preparation was conducted by J.A.H. Data analysis and processing
692 was conducted by J.A.H., A.H., and M.L. J.A.H., J.A.D, E.R.H. and M.L. discussed data and provided
693 critical input. J.A.D., E.R.H. and M.L. prepared the manuscript. All authors read and commented on the
694 manuscript.

695

696 **Ethics declaration**

697 Competing interests

698 All authors declare no competing interests.

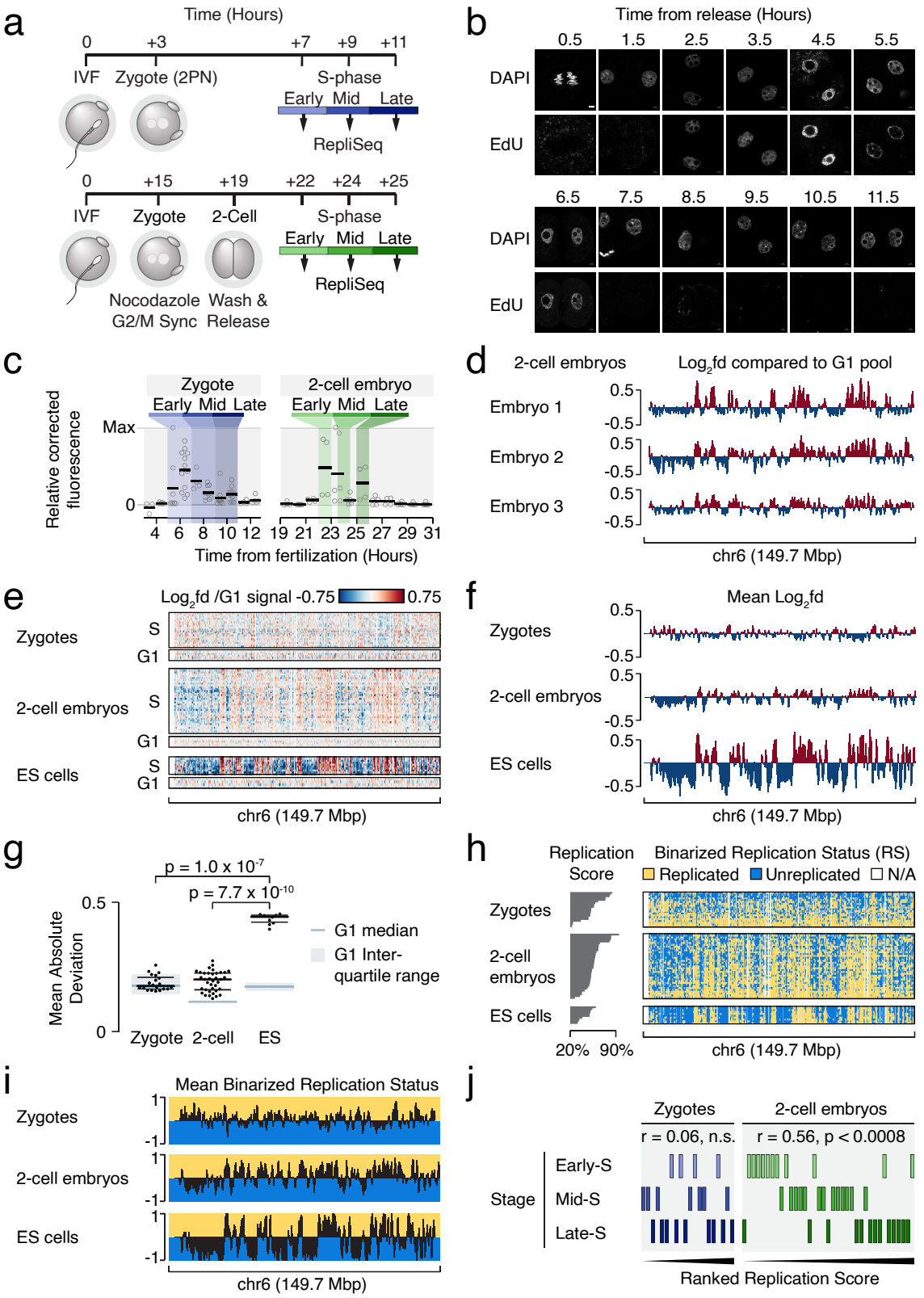

Single-embryo Repli-seq reveals atypical replication timing in zygotes and 2-cell embryos

a) The schematic illustrates the procedure and timing for obtaining mouse zygotes and 2-cell embryos undergoing DNA replication. In the upper panel, zygotes were selected at different times during the S phase after fertilization. In the lower panel, Nocodazole was utilized to synchronize the release of 2-cell embryos into the second cell cycle.

b) Microscopy of EdU pulse labelling of mouse 2-cell embryos at indicated time points after release from Nocodazole-induced inhibition of mitosis. Scale bar = 5µM.

c) Quantitation of EdU-incorporation in mouse zygotes and 2-cell embryos at indicated time points after fertilization. Coloring illustrates the time points defined as Early, Mid, and Late parts of the S-phase.

d) Graphs showing normalized Repli-seq read densities of three S-phase 2-cell embryos at chromosome 6. Values are log2-fold differences relative to the G1-phase signal.

(*Continues on next page*)

e, f) The heatmap (**e**) and graph (**f**) display normalized Repli-seq read densities in S- and G1-phase mouse zygotes, 2-cell embryos, and ESCs on chromosome 6. The heatmap shows individual embryos, while the graph represents mean values. The values are presented as log2-fold differences relative to the G1-phase signal for each cell type.
g) Beeswarm plots of the mean absolute genome-wide deviation in each Repli-seq sample. The background deviation from G1 controls for each sample is indicated with grey boxes and wide bars showing the interquartile range and median, respectively. Black bars indicate the 25, 50, and 75 percentiles of the S-phase populations. P-values obtained by two-sided Mann-Whitney U-tests Benjamini-Hochberg corrected for multiple testing.
h, i) Heatmaps of individual binarized replication status values (**h**) and mean binarized Replication status of S-Phase mouse zygotes, 2-cell embryos and ESCs at chromosome 6 (**i**). Binarized values were derived from Repli-seq data normalized to the G1-phase signal for each cell type. The vertical order and left side bar diagram (**h**) reflect the Replication Score for each sample.
j) Tile plot showing relationships between S-phase progression and ranked Replication Score from Repli-seq data in mouse zygotes and 2-cell embryos. r- and p-values were obtained using Spearman's rank correlation tests Benjamini-Hochberg corrected for multiple testing.

Halliwell et al., Figure 2

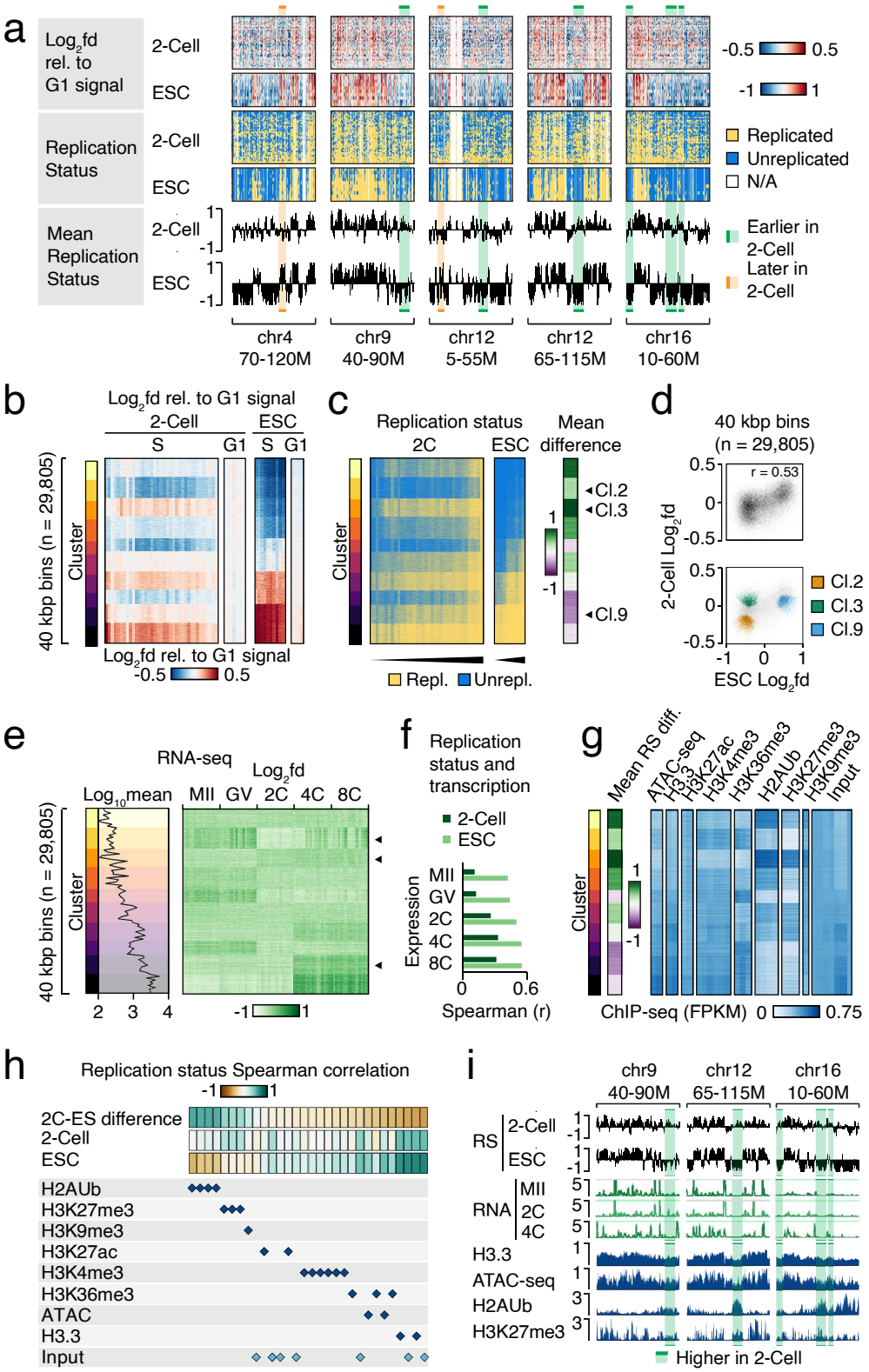

Consistent differences in local replication timing between 2-cell embryos and ESCs

a) Heatmaps showing normalized Repli-seq read densities (upper) and binarized Replication Status (middle) as well as graphs showing mean binarized Replication Status (bottom) of S-phase 2-cell mouse embryos and ESCs at five selected genomic loci. Orange and green highlighted regions indicate loci with marked differences between these cell types.

b) Heatmaps showing the genome-wide signal enrichment and variation in individual Repli-seq samples from S- and G1-phase 2-cell embryos and ESCs. 40 kbp bins that contained signal from both conditions (n = 29,805) were k-means clustered according to the indicated S-phase signal from all individual 2-cell mouse embryos and ESCs. Clusters were ordered according to S-phase ESC signal.

c) Heatmaps showing the genome-wide binarized Replication Status in individual Repli-seq samples from S-phase 2-cell embryos and ESCs ordered as in (**b**). Rightmost heatmap shows differences in the mean binarized Replication Status between 2-cell mouse embryos and ESCs.

(*Continues on next page*)

d) Scatter plots showing the relationship between mean normalized S-phase Repli-seq read densities in mouse ESCs (X-axis) and 2-cell embryos (Y-axis) for all 40 kbp bins (top) or three selected clusters (bottom). R-value indicates the Pearson correlation coefficient.
e) Composite panel showing mean genome-wide transcript density (graph, left) or log2-fold differences relative to the mean (heatmap, right) from single mouse oocyte or embryo RNA-seq[19]. Signal was quantified in 40 kbp bins ordered as in (**b**).
f) Bar diagrams showing the correlation between mean Replication Status from S-phase mouse 2-cell embryos or ES-cells and transcript density from the indicated oocyte and embryo stages. The signal was analyzed in 40 kbp bins and correlation was measured using Spearman rank correlation tests.
g) Heatmaps showing genome-wide histone marks, histone variant, and chromatin accessibility signal from mouse oocytes. Signal was quantified in 40kbp bins ordered as in (**b**) and FPKM-normalized. Leftmost heatmap shows mean Replication status differences as in (**c**).
h) Tile plot showing the genome-wide correlation of histone marks, histone variant, and chromatin accessibility data in mouse oocytes (indicated by lowermost blue rhombs) relative to mean Replication Status from S-phase mouse 2-cell embryos, ES-cells, and the difference between these two. The signal was analyzed in 40 kbp bins and correlation measured using Spearman rank correlation tests.
i) Genome-browser tracks of mean binarized Replication Status (top, black), RNA-seq (middle, green), histone mark and chromatin accessibility (bottom, blue) at example loci with relatively early 2-cell replication (highlighted in green).

Halliwell et al., Figure 3

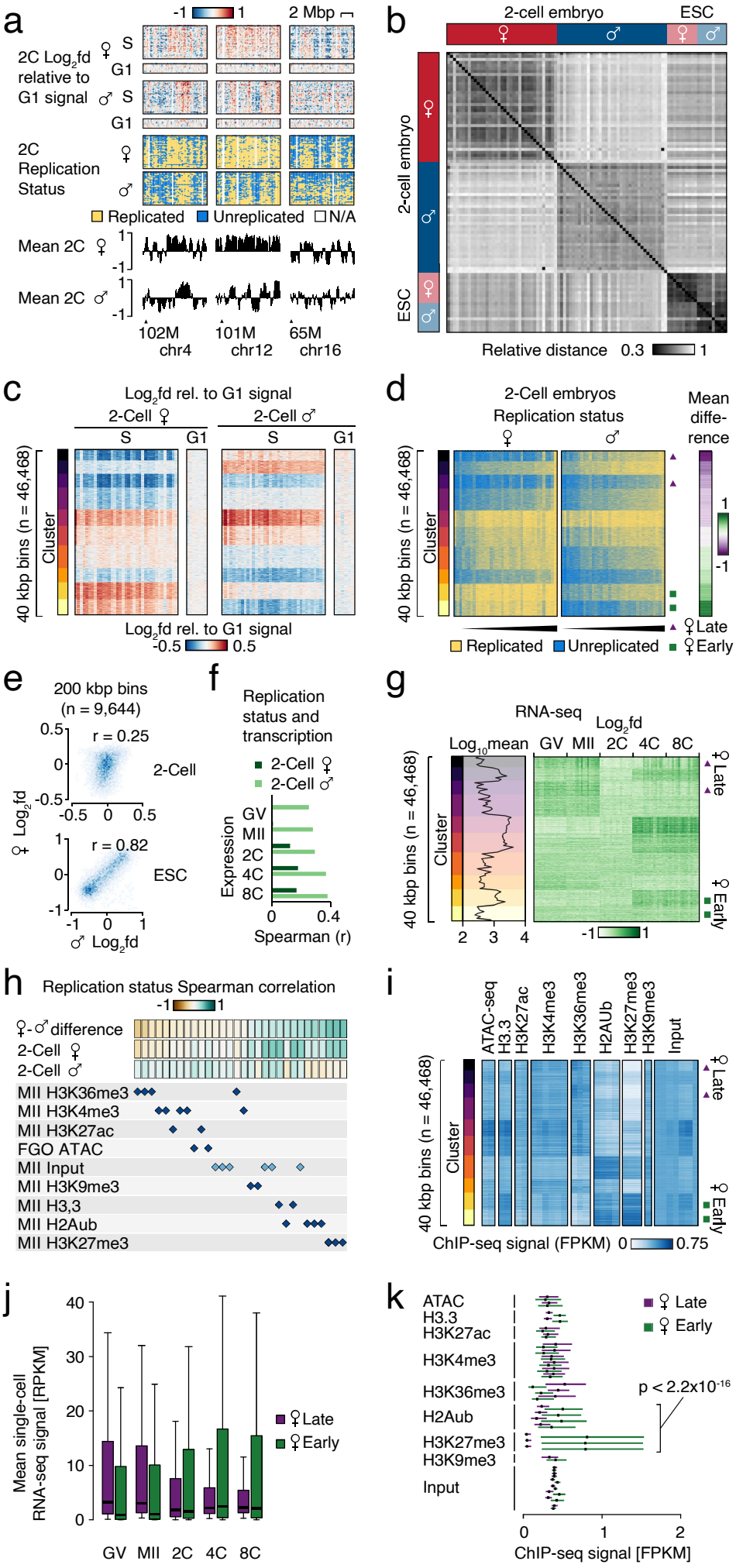

Halliwell et al., Figure 3 Legends

Abundant local parental differences in the replication timing of 2-cell embryos

a) Heatmaps showing normalized Repli-seq read densities (upper) and binarized Replication Status (middle) as well as graphs showing mean binarized Replication Status (bottom) of S-phase of the maternal and paternal genome in 2-cell mouse embryos at selected genomic loci.

b) Distance matrix of showing the relative Euclidian distances between Repli-seq enrichment profiles of maternal and paternal genomes in individual mouse 2-cell (n=37) and ESC samples (n=20).

c) Heatmaps showing the genome-wide signal enrichment and variation in individual Repli-seq samples from the maternal and paternal genome of S- (n=37) and G1-phase (n=7 Maternal, n=6 Paternal) 2-cell mouse embryos. 40 kbp bins that contained signal from both haplotypes (n = 46,468) were k-means clustered according to the indicated S-phase signal from all individual maternal and paternal samples. Clusters were ordered according to the mean difference between the maternal and paternal signal.

d) Heatmaps showing the genome-wide binarized Replication Status in individual Repli-seq samples from the maternal and paternal genome of S-phase 2-cell mouse embryos ordered as in (**c**). Rightmost heatmap shows differences in the mean binarized Replication Status between the maternal and paternal genomes. Green squares and purple triangles indicate selected clusters constituting subpopulations of regions with a notably early or late replication of the maternal genome, respectively.

e) Scatter plots showing the genome-wide relationship between mean normalized S-phase Repli-seq read between the paternal (X-axis) and maternal (Y-axis) genomes for mouse 2-cell embryos (top) or ESCs (bottom) analyzed in 200 kbp bins. R-values indicate Pearson correlation coefficients.

f) Bar diagrams showing the correlation between mean Replication Status from the maternal and paternal genome of S-phase 2-cell mouse embryos and transcript density from the indicated oocyte and embryo stages. The signal was analyzed in 40 kbp bins and correlation measured using Spearman rank correlation tests.

g) Heatmaps showing transcript density difference from single mouse oocyte or embryo RNA-seq[19] Signal was quantified in 40kbp bins ordered as in (**c**) and FPKM-normalized. Green squares: maternal early replicating, purple triangles: maternal late replicating, defined in (**d**).

h) Tile plot showing the genome-wide correlation of histone mark and chromatin accessibility in mouse oocytes (indicated by lowermost blue rhombs) relative to mean Replication Status from the maternal and paternal genome of S-phase 2-cell mouse embryos as well as the difference between these two. The signal was analyzed in 40 kbp bins and correlation measured using Spearman rank correlation tests.

i) Genome-wide histone mark and chromatin accessibility signal from mouse oocytes with mean Replication status of the 2-cell embryos and ESC. Signal was quantified in 40kbp bins ordered as in (**c**) and FPKM-normalized. Green squares: maternal early replicating, purple triangles: maternal late replicating, defined in (**d**).

j) Box plots showing transcript densities at 40 bins within the maternal early and late replicating subpopulations. Whiskers represent the 1.5x interquartile range and the bar is the median value.

k) Plot of upper and lower quartiles as well as medians (black vertical bars) of histone marks, histone variants, and chromatin accessibility signal from mouse oocytes quantified at 40 kbps within the maternal early and late replicating subpopulations defined in (**d**). P-values obtained by two-sided Mann-Whitney U-tests Benjamini-Hochberg corrected for multiple testing

Halliwell et al., Figure 4

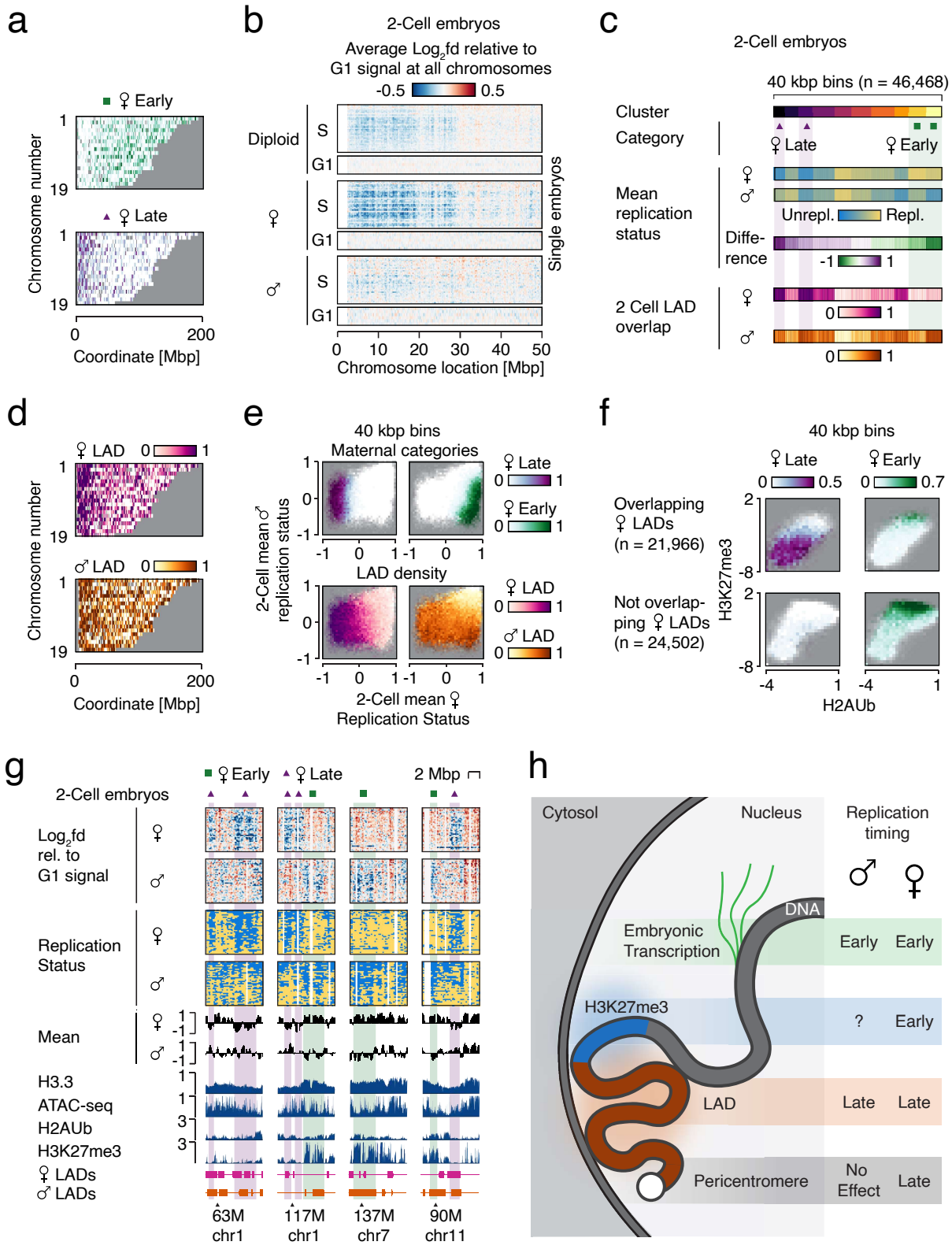

Maternal replication timing is associated with nuclear compartmentalization and epigenetic marks

a) Heatmaps showing the density of maternal early (upper) and late (lower) replicating regions, defined by the genome-wide binarized replication status (figure **3d)**. X-axis position correspond to chromosome coordinates, and Y-axes correspond to autosome number. Centromere is positioned at 0 Mbp.

b) Heatmaps showing the average enrichment at all chromosomes from individual Repli-seq samples from the diploid (top), maternal (middle) and paternal (bottom) genome of S- and G1-phase 2-cell mouse embryos. X-axis position correspond to chromosome coordinates, and Y-axes depict to individual samples.

c) Heatmaps of genome-wide mean binarized Replication Status and difference (middle) and lamin-associated domains (LAD) density in the maternal and paternal genomes of S-phase 2-cell mouse embryos (bottom) at clusters defined in Figure **3c**.

d) Heatmaps showing the density of maternal (upper) and paternal (lower) LADs in 2-cell mouse embryos. X-axis position correspond to chromosome coordinates, and Y-axes correspond to autosome number.

(*Continues on next page*)

e) Heatmaps showing the density of maternal late (upper left) and early (upper right) replicating regions, defined in figure **3d**, as well as the density of maternal (lower left) and paternal (lower right) LADs in 2-cell embryos relative to mean maternal (X-axis) and paternal (Y-axis) binarized Replication Status.
f) Heatmaps showing the density of maternal late (left) and early (right) replicating regions, defined in figure **3d**, within (top) or outside (bottom) LADs in the maternal genome of 2-cell mouse embryos relative to mean enrichment of the H2AUb (X-axis) and H3K27me3 (Y-axis) histone marks in mouse MII oocytes.
g) Heatmaps and genome-browser tracks Repli-seq of the maternal and paternal genome in 2-cell S-phase mouse embryos in relation to various features at selected loci. From top: heatmaps of normalized Repli-seq read densities, heatmaps of binarized Replication Status, graphs of mean binarized Replication Status, histone mark, histone variant, and chromatin accessibility in mouse oocytes, maternal and paternal LADs in 2-cell mouse embryos. Regions highlighted in green and orange indicate maternal early and late replication, respectively.
h) Schematic illustration of identified relationships between maternal and paternal replication timing in 2-cell embryos and key genomic features.